Modeling the acquisition front-end in high resolution gamma-ray imaging

Pedro Guerra, *Student Member IEEE*, Juan E. Ortuño, Juan José Vaquero, *Senior Member IEEE,*
George Kontaxakis, *Member IEEE,* Manuel Desco, Andrés Santos, *Senior Member IEEE*

Abstract— **The availability of synthetic realistic data enables design optimization, algorithm evaluation and verification of any digital system where a significant amount of digital signal processing is performed. The evolution of positron emission tomography cameras towards continuous sampling of individual position-sensitive photomultiplier anodes with processing algorithms implemented on digital programmable logic devices creates a new framework where new approaches to the γ-event detection are possible. We have developed a system model of the acquisition chain, including multi-layer phoswich, photomultiplier, front-end analog electronics, data acquisition and data processing. This processing includes estimation algorithms for the most relevant event parameters: energy, layer-of-interaction, time picking-off and event location. The selected simulation platform couples gently to digital hardware simulation tools, in such a way that implemented models may generate real-like stimuli for the digital system under development. The modeling of the whole front-end electronics enables deeper understanding and tuning of different system trade-offs and provides a rapid and soft transition between specification and hardware development.**

Keywords: continuous sampling, depth of interaction, front-end electronics, nuclear pulse processing, hardware validation, positron emission tomography (PET) modeling.

I. INTRODUCTION

IMAGE quality in positron emission tomography (PET) is strongly influenced by the gamma detector capability to estimate energy, timing and positioning of the γ-event. Traditionally gamma rays are detected by scintillator crystals, that produce a scintillated light pulse which is amplified, commonly by a position-sensitive photomultiplier tube (PS-PMT), and readout via charge division techniques [1, 2]. Recent experimental results have shown that processing of individual PS-PMT channels might provide better position estimation and image quality, at the cost of higher complexity and more supporting electronics [3]. Spatial resolution and resolution uniformity can be further improved reducing the parallax error by means of considering a multi-layer detector [4], also known as phoswich.

In this work the system to be modeled consists of a multi-layer detector coupled to a PS-PMT, whose anode outputs are further processed and read by free running analog-to-digital converters (ADCs) at a given acquisition frequency f_s. Dedicated digital logic processes and characterizes the detected pulses. The motivation to investigate this architecture is the higher spatial resolution and uniformity resolution that can be achieved when the system is able to identify the depth-of-interaction (DOI) [5] in real time, combined with the potential benefits of performing digital processing on each individual channel to increase signal-to-noise ratio and improve position estimation, via local energy integration. Such scheme may also improve timing resolution by means of correcting transit time differences among channels before energy integration and pulse processing.

This work focuses on modeling both system front-end electronics as well as the digital processing algorithms. This approach eases system internal characteristics understanding, facilitating the optimization of the design of future PET detector modules [6]. In addition, algorithms estimating pulse parameters such as energy, positioning or timing are implemented, being validated and evaluated via cosimulation using simulated realistic synthetic pulse as input stimuli to the HW under development.

II. METHODS

A. Simulation platform

The analog front-end (crystal layers, PS-PMT, analog electronics and ADCs) and the digital signal processing algorithms have been modeled using Simulink 5.0 (The Mathworks, Natick, MA, USA). Modeling of the processing algorithms have been realized with a HW implementation in mind.

Additionally these algorithms have been implemented as digital blocks described with synthesizable VHDL (Very High

P.Guerra, J.E. Ortuño, G. Kontaxakis and A. Santos are with the Electronic Engineering Department, Universidad Politécnica, Madrid, Spain E-20040
e-mail: pguerra, juanen,gkont,andres@die.upm.es
J.J.Vaquero and M.Desco are with the Hospital General Universitario Gregorio Marañón, Madrid, Spain E-28007
e-mail: juanjo,desco@mce.hggm.es

Speed Integrated Circuit Hardware Description Language) optimized for their implementation on programmable logic (FPGA) from Xilinx (Xilinx, San José CA, USA), and their functionally has been simulated with Modelsim SE (Mentor Graphics, Wilsonville, USA). The software package *XtremeDSP®* from Xilinx has been used for the VHDL code verification and performance estimation. This package provides the coupling between Simulink and Modelsim, where the first provides both realistic stimuli and the analysis tools while the latter simulates the accurate behavior of the synthesized hardware. Code evaluation and performance estimation are based on several set-ups (testbenches) which intensively exercises the different sub-modules.
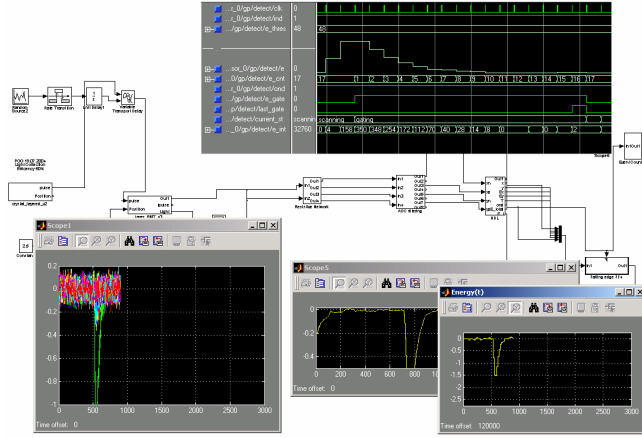

Fig.1: The simulation platform consists of Simulink and Modelsim cosimulating different aspects of the system. It this figure a feasible set up is shown, with the testbench being simulated at the background, and some signal probes, including a HDL waveform, in the foreground.

B. System Model

Synthetic anode pulses are built by modeling the different stages of the acquisition chain, taking into account the statistical properties of the processes involved. The starting point is the average charge $\overline{Q_o}$ delivered by each anode of the photomultiplier, which may be computed as:

$$\overline{Q_o} = \overline{N}_{PHO} \cdot \eta \cdot \overline{G} \tag{1}$$

where $\overline{N}_{PHO}$ is the mean number of photons created in the scintillator upon γ-absorption, η represents the probability that an optical photon from the scintillator reaches the first dynode of the PS-PMT and G represents the mean electron multiplication factor of the PS-PMT [7]. This charge is delivered in the form of a current pulse, which after preprocessing can be acquired and analyzed by the digital electronics.

Crystal Model

On every γ-ray scintillator interaction there is an energy exchange which generates as a result a certain amount N_{PHO} of optical photons. The actual number of generated photons is function of the γ-ray energy E_γ, the scintillator photoelectric fraction P_{FE}, the photon yield $Y(E_\gamma)$ and the scintillator intrinsic energy resolution $\Delta E/E$.

Moreover these photons are time distributed according to the scintillation properties of the crystal, which can be modeled as a lineal combination of two or more exponential functions [8], which take into account pulse rise τ_{RISE} and fall τ_{FALL} constants. Most scintillators of interest may be described with a single rise and a single fall constant [6], therefore the crystal pulse is modeled as follows:

$$E_{CRISTAL} = \begin{cases} E_\gamma = h\nu & \text{with Prob}(P_{FE}) \\ U\left(0, \dfrac{E_\gamma^{\,2}}{E_\gamma + 255}\right) & \text{with Prob}(1 - P_{FE}) \end{cases} \quad [9] \tag{2}$$

$$N_{PHO} = N\left(E_{CRISTAL} \cdot \text{Yield}, \frac{\Delta E}{E_{CRISTAL}}\right) \tag{3}$$

$$N_{PHO}(t) = N_{PHO}\, \frac{\exp\left(-t/\tau_{FALL}\right) - \exp\left(-t/\tau_{RISE}\right)}{\tau_{FALL} - \tau_{RISE}} \tag{4}$$

where $U(a,b)$ stands for a uniform distribution between a and b, and $N(m,v)$ stands for a gaussian distribution with mean m and variance v.

The second term η of equation (1) is decomposed as the product of two terms: crystal efficiency η_{CRYS}, which ranges between 20-60% depending on crystal size, surface finish and coupling to the PMT [10], and the quantum efficiency η_{PMT}, which depends on PMT efficiency at the wavelengths defined by the scintillator emission spectrum and is usually less than 25%. They are implemented as a binomial distribution, where a the actual number of photons $N'_{PHO}(t)$ that at a given time point t reaches the photocathode is:

$$N'_{PHO}(t) = \arg n\{U(0,1) == P(n|N_{PHO}(t))\}$$

$$P(n|N_{PHO}(t)) = \binom{N_{PHO}(t)}{n} \cdot \eta^n \cdot (1-\eta)^{N_{PHO}(t)-n} \tag{5}$$

In case of a multi-layer phoswich, in first place the crystal layer is selected randomly, taking into account the *a priori* probabilities of each layer which are function of crystal lengths and the scintillator stopping power, and next a pulse is drawn out as described in previous equations (2)(3)(4)(5).

PS-PMT Model

The next item in the chain is the PMT, whose basic functional diagram is shown in fig.2. It consists of a photocathode and a series of dynodes in an evacuated glass enclosure. When photons strike the photocathode, electrons are emitted via the photoelectric effect. The electrons are focused onto the first dynode by an electric field and when they strike the dynodes, more electrons are emitted. The current of electrons increases as it moves down the successive dynodes until it reaches the anode, producing a small current pulse, achieving an amplification gain of 10^3-10^8. The voltage divider network shown in the figure carries a steady current $-HV/R_{tot}$ which supplies the electrons for multiplication at each dynode.
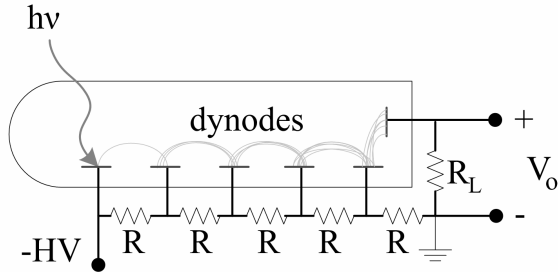

Fig. 2. Schematic of a basic photo multiplier. When operating the PMT, a high voltage(HV) is applied over the photocathode, the dynodes and the anode. This is done by the aid of a resistor chain that creates a potential ladder down the structure. When a photon hν from a scintillating crystal enters the PMT window it will hit the photocathode and there is a certain probability (given by the quantum efficiency) that an electron is emitted under the action of the photoelectric effect.

PMT's use is widely spread mostly because of their high linearity and gain. The most important parameters are the gain, which is function of voltage and temperature, dark current, transit time, rise time as well as cross-talk and gain non-uniformities. The implemented PMT simulation model extends the statistical approach presented at [11] to a PS-PMT, where each cathode collects and amplifies the energy striking a particular section of the PMT surface.
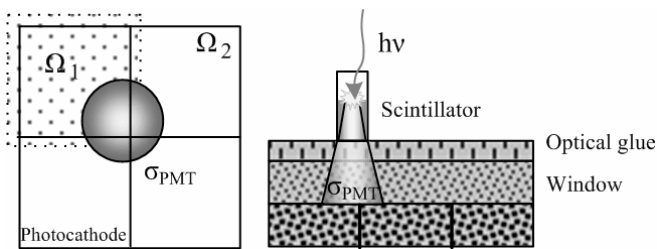

Fig. 3. The scintillation light pulse from a given crystal irradiates an area of the PMT surface, which includes several photocathodes. Each of these collects and amplifies the energy, giving away a current pulse through its anode that is function of the impact location, PMT properties.

As it is shown in the Fig.3 the photons coming out the crystal illuminate an area of the photocathode bigger than the crystal section due to the photon spread during their propagation through the optical glue and borosilicate window.

This spread has been modeled as a spatially distributed gaussian function centered at the crystal whose spread factor σ_{PMT} is empirically determined. In this way the energy collected by each anode j is computed as the integral across the corresponding cathode domain Ω_j as follows:

$$F_j = \frac{G_j}{\sqrt{2\pi\sigma_{PMT}^2}} \int_{\Omega_j} \exp\left(-\frac{(x-x_m)^2+(y-y_m)^2}{2\sigma_{PMT}^2}\right)\cdot dx\cdot dy \qquad (6)$$

where (x_m, y_m) are the coordinates of the m crystal center at which energy deposition takes place, G_j includes gain non-uniformities and σ_{PMT} models photon spread.

Finally the single-photon PMT response, characterized by the device's rise time $t_{PMTrise}^2$ and transition time jitter $t_{PMTjitter}^2$, is modeled as:

$$h(t) = \frac{1}{t_p^2}\cdot t\cdot\exp\left(-\frac{t}{t_p}\right)$$

$$t_p^2 = t_{PMTrise}^2 + t_{PMTjitter}^2 \qquad (7)$$

Combining all this expressions together the current $i_j(t)$ at the output of each anode j is estimated as the PMT response to the photon flux illuminating the cathode plus the dark current I_{dark} as follows, where $\overline{G}$ is the PMT gain, T is the simulation time step and q is the charge of an electron:

$$i_j(t) = \frac{q}{T}\cdot\overline{G}\cdot F_j\cdot h(t)*N'_{PHO}(t) + I_{dark} \qquad (8)$$

Readout Model

Two options are considered for anode readout; on one side, the classical Anger approach where the number of processed signals is reduced by means of a resistive network [1], on the other all anodes are individually acquired [12]. In any case current pulse is amplified by a transimpedance filter and shaped by a $CR-RC^n$ filter[13] prior to digital conversion by an analog-to-digital converted (ADC) sampling at a fix rate f_s. The acquired stream will be digitally processed to identify and characterize the pulses generated by the detected γ-ray.

At this point it is required to stress the considered noise model, as it is essential to achieve a realistic synthetic pulse. In the implemented models both series e_n^2 and parallel i_n^2 noise are considered as described in fig.4. It has been shown [14] that under normal conditions the noise spectral density may be modeled as a first polynomial, where the coefficients a, b, a_f, b_f are either analytically estimated or empirically computed:

$$\frac{de_n^2}{df} = a + \frac{a_f}{|f|}$$

$$\frac{di_n^2}{df} = b + b_f|f|$$

(9)
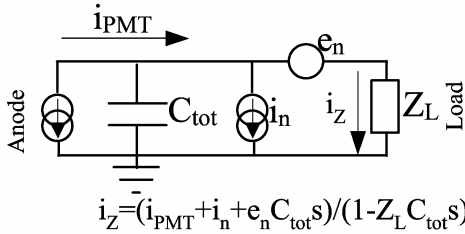
$$i_Z = (i_{PMT} + i_n + e_n C_{tot}s)/(1 - Z_L C_{tot}s)$$

Fig. 4: Noise model for the analog front-end. It is important to point out the influence of parasitic capacitances C_{tot} on the series noise e_n which may dominated over the rest of noise sources.

III. RESULTS

The presented models for the analog front-end have been implemented as parametrizable Simulink blocks, that are easily configured to simulate different scenarios or testbenches. The first of these scenarios mimic an available LYSO-based detector whose pulses are compared, as shown in Fig.5, to real dynode pulses acquired with an oscilloscope. As it can be seen, both shape and noise level are identical.
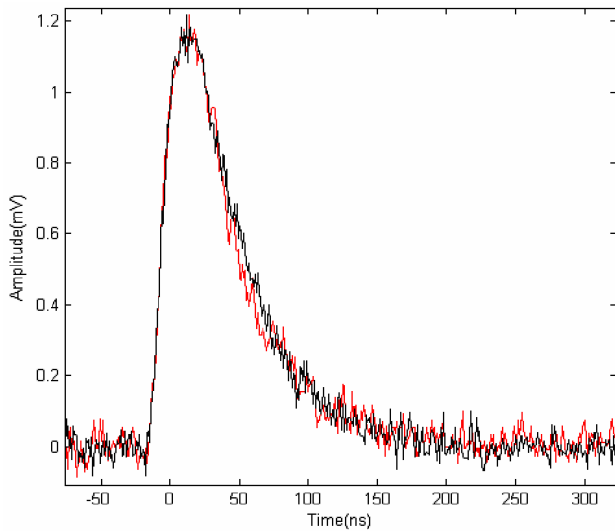

Fig. 5: Real(red) versus synthetic(black) LYSO (Crystal Photonics Inc) pulse.

The next stage has been the configuration of the Simulink blocks to model the analog front-end consisting of a 16x16 LSO(0.22x0.22x1.2cm)/GSO(0.22x0.22x1.2cm) phoswich coupled to a Hamamatsu H5000 PS-PMT[17] with optical grease, based on the observations and measurements carried out by several authors [3][5][7][12][15][16][18]. Given the scintillator, coupling and PMT properties the overall efficiency η is set to 10% which is consistent with previously reported values [7],[19]. Noise levels are set based on the measurements done with our current front-end. Anode outputs are reduced to 4 Anger signals namely (X+,X-Y+Y-) by means

of a resistive network[1], each of which is filtered by a CR-RC filter with 10 ns peaking time and continuously sampled at 50MHz. Finally, the original PMT has been simplified from 8x8 to 4x4 channels in order to speed-up simulations and provide a pessimistic scenario for performance estimations.
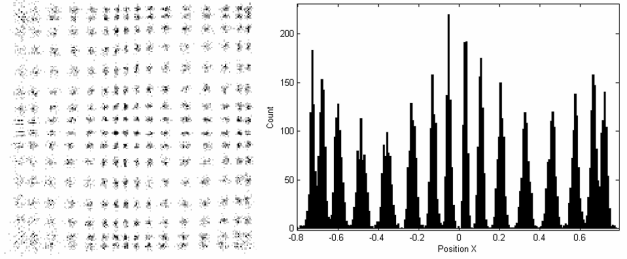

Fig. 6: Simulated flood map (left) for an LSO-only simulation with Anger positioning. Distortions are due to crystal lower light collection near the edges, the non-uniform gain of the PS-PMT and non-linearities introduced by the resistive network. The profile on the x-axis (left) shows that despite distortions the 16 crystals can still be identified.
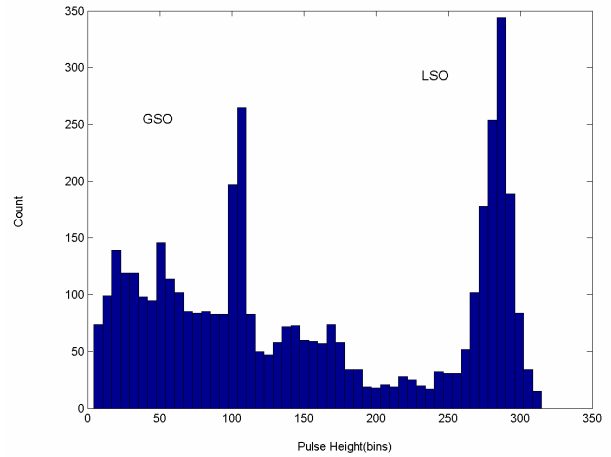

Fig. 7: Simulated energy spectrum for fixed crystal. GSO and LSO 511KeV photopeaks are clearly identified. The FHWM energy resolution is estimated to be around 15.5% for GSO and 11.5% for LSO. The relative gain between LSO and GSO is 2.7:1, as expected due to the lower GSO photon yield and slightly lower PS-PMT quantum efficiency at the GSO wavelength.

The data stream generated by the ADC models is used as input stimuli to the VHDL code which is concurrently simulated by Modelsim. These stimuli have been used to debug and validate the implemented digital algorithms: pulse detection, energy, position, time stamp generation and pulse shape for DOI estimation.

Fig. 6 shows a simulated flood map for a LSO-only simulation and the x-axis profile. Distortions on the crystal location may be attributed to the crystals lower light collection near the edges, the non-uniform gain of the PS-PMT and non-linearities introduced by the resistive network.

Event position, Fig 6, and energy, Fig 7, are estimated by triggering acquisition when the energy goes above a fix threshold and accumulating the samples for a given integration window. Crystal identification is based on delay integration [5] [20] where, as shown in fig. 8, the classification error rate is

estimated to be below 10%. Finally timestamps are obtained by zero-crossing a filtered [21] version of the input energy achieving an estimated single timing resolution (FWHM) around 1.8 ns for LSO and 5 ns for GSO.
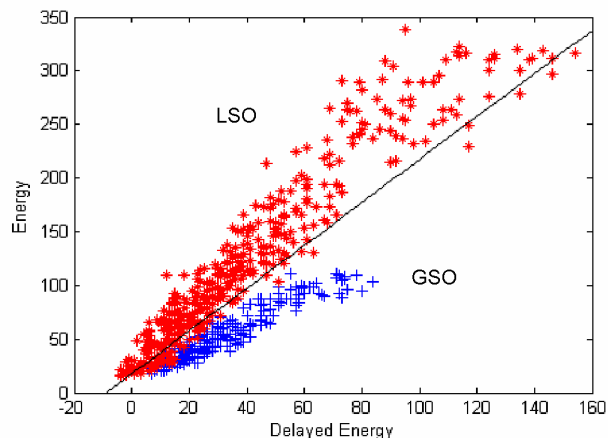

Fig. 8: Simulated phoswich diagram for LSO and GSO. The y-axis is the result of integrating the complete pulse energy while in the x-axis only a few samples of the pulse tail are integrated. Due to HW implementation both energies are related with a scale factor of 4.

IV. CONCLUSIONS AND FUTURE WORK

Our simulation results show very good agreement with published results for similar configurations [3], [18] and suggest that this relatively simple system models are able to describe the most significant system features and provide realistic stimuli to the VHDL, fact that eases the implementation and validation of the implemented algorithms on hardware as well as enables the estimation of system performance. As an example, the availability of synthetic stimuli gave valuable insight for the design and optimization of the digital timestamp generation block and allowed for the detection of a very subtle code bug which would have been very difficult otherwise.

The implemented blocks estimate the most significant parameters of the pulse: energy, position, timestamp and DOI, assuming a continuous data stream generated by free running ADC. As future work, we are currently working on the elaboration of a prototype where pulse will be acquired up to 65MHz, characterized by the processing logic and sent to the host via a Ethernet connection. Additionally we are working on a new VHDL code that takes as input each anode output so that we get rid of the resistive network, and the presented cosimulation environment will be extensively used for debugging, validation and performance estimation.

V. REFERENCES

[1] S. Siegel, R. W. Silverman, Y. Shao, and S. R. Cherry, "Simple charge division readouts for imaging scintillator arrays using a multi-channel PMT" *IEEE Trans. Nucl. Sci.*, vol. 43, pp. 1634-1641, 1996.
[2] V. Popov, S. Majewski, A. G. Weisenberger, and R. Wojcik, "Analog readout system with charge division type output" in *IEEE NSS.*, 2001.
[3] F. Habte, P.D. Olcott, C.S. Levin, A.M. Foundray, and J. A. Talcott, "Prototype Parallel Readout System for Position Sensitive PMT based Gamma Ray Imaging System" presented at *IEEE MIC*, Portland (USA), 2003.
[4] J. Seidel, J. J. Vaquero, and M. V. Green, "Resolution uniformity and sensitivity of the NIH ATLAS small animal PET scanner: Comparison to simulated LSO scanners without depth-of-interaction capability" *IEEE Trans. Nucl. Sci.*, vol. 50, pp. 1347-1350, 2003.
[5] J. Seidel, J. J. Vaquero, S. Siegel, W. R. Gandler, and M. V. Green, "Depth identification accuracy of a three layer phoswich PET detector module" *IEEE Trans Nucl Sci*, vol. 46, pp. 485-490, 1999.
[6] A. Thon, K. Fiedler, T. Frach, W. Rütten, and T. Solf, "Exact Modeling of Analog Pulse for Detector Modules" presented at *IEEE MIC*, Portland (USA), 2003.
[7] P. Dorenbos, J. T. M. de Haas, and C. W. E. van Eijk, "Non-proportionality in the scintillation response and the energy resolution obtainable with scintillation crystals" *IEEE Trans. Nucl. Sci.*, vol. 42, pp. 2190-2202, 1995.
[8] M. e. Ljungberg and M. A. e. King, *Monte Carlo Calculations in Nuclear Medicine : Applications in Diagnostic Imaging*. Philadelphia (USA) : Institute of Physics Publishing, 1998.
[9] J. A. Sorenson and M. E. Phelps, *Physics in Nuclear Medicine*, 2ed. Orlando, Florida (USA): Harcourt Brace Jovanovich, 1987.
[10] C. S. Levin and F. Habte, "Initial studies of a new detector design for ultra-high resolution positron emission tomography" in *IEEE NSS*, 2002.
[11] Burle (1989), "Photomultiplier Handbook" [Online] available http://www.burle.com/cgi-bin/byteserver.pl/pdf/Photo.pdf
[12] S. Riboldi, J. Seidel, M. Green, J. Monaldo, J. Kakareka, and T. Pohida, "Investigation of Signal Readout Methods for the Hamamatsu R8500 Flat Panel PSPMT" presented at *IEEE MIC*, Portland (USA), 2003.
[13] J. Wulleman, "Detector-noise suppression by appropriate CR-(RC)n shaping" *Electronics Letters*, vol. 32, pp. 1953-1954, 1996.
[14] G. Bertuccio and A. Pullia, "A method for the determination of the noise parameters in preamplifying systems for semiconductor radiation detectors" *Review of Scientific Instruments*, vol. 64, pp. 3294-3298, 1993.
[15] M. Moszynski, T. Ludziejewski, D. Wolski, W. Klamra, and V. V. Avdejchikov, "Timing properties of GSO, LSO and other Ce doped scintillators" *Nucl. Instrum. Methods*, vol. 372, pp. 51-58, 1996.
[16] R.P. Pani, R., Cinti, M.N., Trotta, C., Trotta, G., Scafe, R., D'Addio, L., Iurlaro, G., Montani, L., Bennati, *et al* "Factors affecting flat panel PMT calibration for gamma ray imaging" in *IEEE NSS*, 2002.
[17] Hamamatsu (2003), "H8500 Datasheet", [Online] available http://sales.hamamatsu.com/index.php?id=13195715
[18] R. Pani, R. Pellegrini, M. N. Cinti, M. Mattioli, C. Trotta, L. Montani, G. Iurlaro, G. Trotta, L. D'Addio, and S. Ridolfi, "Recent advances and future perspectives of position sensitive PMT" *Nucl. Instrum. Methods*, vol. 213, pp. 197-205, 2004.
[19] W. W. Moses and S. E. Derenzo, "Prospects for time-of-flight PET using LSO scintillator" *IEEE Trans. Nucl. Sci.*, vol. 46, pp. 474-478, 1999.
[20] M. B. Streun, G. Larue, H. Saleh, H. Zimmermann, E. Ziemons, K. Halling, H., "Pulse shape discrimination of LSO and LuYAP scintillators for depth of interaction detection in PET" *IEEE Trans. Nucl. Sci.*, vol. 50, pp. 344-347, 2003.
[21] E. Geraniotis and H. Poor, "Robust Matched Filters for Optical Receivers" *IEEE Trans. Communications,* vol. 35, pp. 1289-1296, 1987.